E×B flow driven electron temperature bifurcation in a closed slot divertor with ion B×∇B away from X-point in the DIII-D tokamak

X. Ma[1], H.Q. Wang[1], H. Y. Guo[2], A. Leonard[1], R. Maurizio[3], E.T. Meier[4], J. Ren[5], P. C. Stangeby[6], G. Sinclair[1], D.M. Thomas[1], R.S. Wilcox[7], J.H. Yu[1], J. Watkins[8]

[1]*General Atomics, PO Box 85608, San Diego, CA 92186-5608, United States of America*

[2] ENN Group, Hebei, China[3]

[3] *Oak Ridge Associated Universities, 100 ORAU way, Oak Ridge, TN 37830, United States of America*

[4] *Zap Energy Inc., Smith Tower, 506 Second Avenue, Seattle, WA 98104, United States of America*

[5] *University of Tennessee Knoxville, Knoxville, TN 37996, USA*

[6] *University of Toronto, 4925 Dufferin St., Toronto, M3H 5T6, Canada*

[7] *Oak Ridge National Laboratory, PO Box 2008 Oak Ridge, TN 37831, USA*

[8] *Sandia National Laboratories, Albuquerque, NM, USA*

An electron temperature bifurcation is observed in the small angle slot (SAS) divertor, which has been developed to enhance neutral cooling across the divertor target by coupling a closed slot structure with appropriate target shaping. Experiments in DIII-D and associated SOLPS-ITER modeling with full drifts find a strong interplay between drifts and divertor geometry in facilitating divertor dissipation. The coupling of divertor geometry and drift flows can strongly affect the path towards divertor detachment onset as the plasma density is raised. With the strike point on the inner slanted surface and ion **B**×∇B away from the magnetic X-point, bifurcative transitions were observed with sharp decrease of T_e towards detachment onset both experimentally and computationally. This differs from the situation for the open divertor where the T_e cliff was only observed for ion **B**×∇B towards the X-point. SOLPS-ITER modeling with full drifts demonstrates that the magnitude of the **E**×**B** drift flow is comparable with the main plasma flow. The reversal of both the poloidal and radial **E**×**B** flows near the strike point leads to rapid density accumulation right near the separatrix, which results in bifurcative step transition of divertor conditions with cold plasma across entire divertor target plate. These results indicate that the interplay between geometry and drifts should be fully taken into account in future fusion reactor divertor designs.

1. Introduction

Development of robust divertor solutions for adequate control of both heat flux and erosion at the targets still remains one of the main challenges to the design and operation of next generation high performance steady-state fusion devices. It requires: divertor target heat load $q_\perp \leq 10-15\ \mathrm{MW/m^2}$, and divertor plasma temperature at the target plate $T_e \leq 5-10$ eV to suppress net erosion [1,2]. This necessitates divertor operation in the detached plasma regime by dissipating most of the power before reaching the divertor targets [3,4]. The present ITER divertor design [5] aims to achieve highly dissipative, detached divertor conditions by operating at a high main plasma density, *i.e.* with a Greenwald density fraction, $n_e/n_G \sim 1$. Thus, the control of detachment is a key element for future high-power long-pulse tokamaks [6].

Extensive effort has been made to develop advanced divertor configurations by optimizing divertor geometry to enhance plasma energy and momentum dissipation by recycling neutrals, leading to more closed divertor configurations [7–11]. On the DIII-D tokamak, a small angle slot (SAS) divertor concept, has been developed on the DIII-D tokamak, based on SOLPS modeling without drift, leveraging the effect of a closed slot structure to enhance neutral trapping inside the divertor and advanced target shaping to tailor the neutral distribution across the target surface [12–14]. First experimental tests and drift-dependent modeling already found a strong interplay between divertor geometry and **E**×**B** drift flows on divertor dissipation [15-17], which is not seen in open divertors.

Bifurcation-like confinement transitions in magnetically confined plasmas have been widely discussed [18,19], in which **E**×**B** drift plays an important role. Such bifurcative step transition is also observed in the DIII-D lower open divertor for operation with normal-B_T (ion **B**×∇B drift pointing towards the magnetic X-point) [20,21]. The formation of this detachment bifurcation has been associated with impurity radiation loss [22], and anomalous cross-field transport [23,24]. Recent modeling with full drifts, using edge plasma codes UEDGE [20] and SOLPS-ITER [25], indicates that the non-linear interaction between **E**×**B** drift flows and divertor electron temperature and plasma potential is the drive for such bifurcated onset of outer divertor detachment in H-mode plasmas in DIII-D.

Here, we report for the first time a similar bifurcation-like transition in divertor plasma conditions in a closed slot diverter in the DIII-D tokamak, mainly driven by **E**×**B** drift flow reversal near the strike point and in the scrape-off layer region. Combined experimental and code-modeling evidence confirms a strong interplay between divertor geometry and **E**×**B** drift flows - which are ubiquitous in magnetic confinement plasmas - on the divertor detachment trajectory in a closed slot divertor, viz. the SAS divertor in DIII-D. It is found that the path towards detachment can be dramatically altered by varying the position of the strike point relative to the target plate of the SAS [17]. With the strike point on the inner slanted surface, a bifurcative transition was observed with target T_e suddenly falling below ~5 eV for both toroidal field directions. This differs from the situation for the open divertor where the T_e cliff was only observed for normal-Bt direction. Detailed SOLPS-ITER simulations with full drifts were able to reproduce the T_e cliff with ion **B**×∇B drift pointing away from the magnetic X-point (favorable direction for lower LH transition threshold), demonstrating the essential role of

E×B drift flows near the strike point in this bifurcative process. This bifurcation observed is strongly coupled to the **E×B** drift flow reversal.

The paper is organized as following. Sec. 2 describes the experiments conducted in the SAS divertor in the DIII-D tokamak and the detailed modeling setups. The experimental data and corresponding modeling results are discussed in Sec. 3. The necessary condition for detachment bifurcation in the modeling is discussed in Sec. 4. Finally, a summary and some conclusions are given in Sec. 5.

2. Experiment and modeling setup

Fig.1 shows the shape of the cross-section of the SAS divertor in DIII-D. The shape of the SAS divertor is optimized for achieving detachment at a relatively lower upstream plasma density based on SOLPS simulations to maximize the neutral concentration in the divertor region. It combines a small target angle in the near scrape-off layer (near-SOL) region and a progressive slot opening toward the far-SOL region [13,14].

Experimental tests of the SAS divertor were carried out systematically in H-mode plasma conditions in DIII-D with plasma current, $I_p = 1$ MA, toroidal field, $B_t = 2$ T, neutral beam heating power, $P_{NBI} = 4.0 - 4.5$ MW, and safety factor q_{95}~4.75. Experiments were performed with several approaches: density scans with fixed strike point to investigate the divertor detachment physics; changing toroidal field direction to investigate the influence of **E×B** drifts on the onset of detachment; strike point sweeping to examine the interplay between divertor geometry and **E×B** drifts. These experiments exploited a comprehensive set of boundary diagnostics, including multiple-channel Thomson scattering (TS) system to obtain electron density and temperature profiles at upstream, target Langmuir probes (LPs) to measure the electron density, temperature, particle flux and inferred-heat flux along the divertor target plates, and surface eroding thermocouples (SETCs) to access the heat flux striking the divertor target.

This paper will only focus on the experiments and corresponding modeling with ion **B×∇B** away from the magnetic X-point and the strike point on the inner slanted surface of SAS, only. The modeling with opposite field direction has not fully reproduced experimental results, specifically the bifurcative transition in divertor plasma conditions. This modeling work is still ongoing and will be reported in a later publication.

The experimental results are benchmarked with drift-dependent modeling using the state-of-the-art boundary plasma code package, SOLPS-ITER [26], the coupled version of the 2D multi-fluid transport code B2.5 [27] and the 3D kinetic neutral transport code EIRENE [28]. The B2.5 fluid code provides the plasma background to EIRENE, while EIRENE computes and returns the source and sink terms for plasma particles, momentum and energy due to plasma-neutral collisions. The simulations were carried out for a deuterium (D) plasma with carbon (C) wall and targets. Simulated particles include ions ($D^+, C^+, C^{+2}, C^{+3}, C^{+4}, C^{+5}, C^{+6}$), atoms (D, C) and molecules (D_2). A complete set of atomic and molecular reactions is included in the modeling, including neutral-neutral collisions. All particle drifts, **E×B, B×∇B,** viscosity and the associated currents are activated in the modeling.

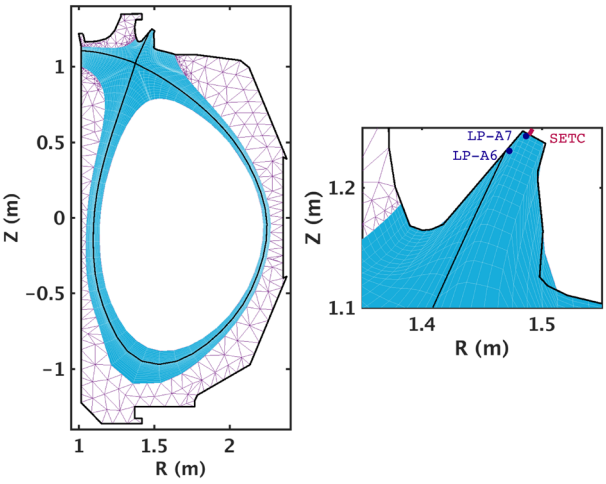

FIG. 1. SOLPS-ITER computational mesh used for the modeling with strike point at the inner slanted surface of the SAS divertor. The positions of two Langmuir probes (LP-A6 & LP-A7) and one of the surface erosion thermocouples are also shown in the left figure.

The computational mesh used in the modeling for the B2.5 code has a resolution of 96×32 and is constructed using the real EFIT [29] plasma equilibrium of shot#179748 at 4000 ms, as shown in Fig. 1. Triangular meshes for the EIRENE code are also shown in Fig. 1. The strike point is placed at the inner slanted surface of the SAS divertor. The solid structure geometry is that of the first wall surfaces of the present DIII-D tokamak, including the SAS divertor. The inherently narrow computational mesh in SAS makes it difficult to reproduce actual DIII-D boundary conditions. As a result, an extended computational mesh is implemented, which required a slight modification to the SAS lower outer corner with more progressive opening [30]. At the core-edge interface, the total power flux is set to 4 MW, shared equally by ions and electrons, to match the power crossing the separatrix for the modeled discharge. A leakage boundary condition is set at the B2.5 grid boundaries for the private flux region and common flux region [31]. A sheath boundary condition is adapted at the boundary of both inner and outer targets, with $V_{//t} + \boldsymbol{V}_{E\times B} \cdot \vec{\boldsymbol{B}}/B = c_s$ [32], where $V_{//t}$ is the parallel plasma flow speed at the target, and $c_s = \sqrt{k_B(T_e + T_i)/m_i}$, the plasma isothermal sound speed. Plasma flux leaving the B2.5 grid is recycled as neutral atoms. The recycling coefficients are set to be 100% at the targets and 99% at the scrape-off layer (SOL) boundary respectively. Both physical sputtering with Roth-Bodhansky yields [33] and fixed 2% chemical sputtering yields are included in the modeling for carbon.

The anomalous cross-field transport coefficients used in the modeling are determined by matching the outer mid-plane (OMP) electron density and temperature profiles from the simulation with experimentally measured upstream profiles from the Thomson Scattering system. In this process, the values of particle diffusivity D and electron thermal diffusivity χ_e are iterated until a satisfactory match is achieved [34]. The ion thermal diffusivity, χ_i, is set to be equal to χ_e, in the absence of good measurements of ion temperature in the SOL region. The calculation was performed using experimental inputs from the reference shot 179838 at 4900ms with an averaged plasma density $\bar{n}_e \approx$

$5.0 \times 10^{19}/m^3$. Fig. 2 (a)(b) show measured electron density and temperature data (red dots) upstream, along with fitted profiles (red solid lines) using a modified hyperbolic function. Profiles from simulations are overplotted with green lines. A good match between experimental profiles and those from simulations is obtained after a few iterations. The calculated cross-field transport coefficient profiles at the OMP are shown in Fig. 2 (c)(d). Both profiles show a well-like shape with minimum values near the separatrix, which is consistent with observations in H-mode plasmas in DIII-D [35,36]. In the divertor region below the X-point, the cross-field transport coefficients are set to be constant across the computational cells, with $D = 0.18\ m^2/s$ and $\chi_e = \chi_i = 0.9\ m^2/s$, the same values as those at the separatrix of the outer midplane.

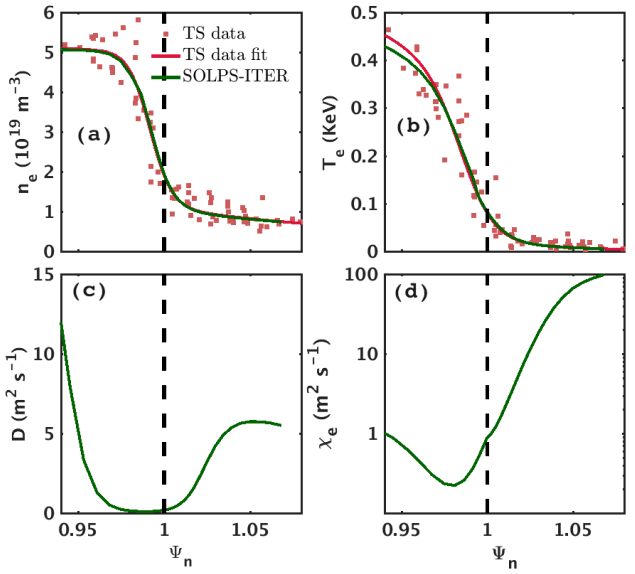

FIG. 2. Electron density (a) and temperature (b) profiles at the outer mid-plane measured by a Thomson scattering system (red dot) for shot#179838 at 5000ms, fitted by a modified hyperbolic function (red solid line), and from corresponding SOLPS-ITER simulation (green solid line). (c) (d) Cross-field anomalous transport coefficients (particle diffusivity and electron thermal diffusivity) for the SOLPS-ITER runs, as determined by the fitting procedure.

4. Results

Fig.3 (a-c) show electron temperature, T_e, and particle flux, J_{sat}, near the strike point measured by target Langmuir probe LP-A6, and deposited heat flux, $q_\perp$, at the slot bottom of the SAS divertor inferred from Langmuir probe LP-A7 and measured by surface thermocouples (SETC), as a function of the upstream outer mid-plane separatrix density, $n_{e,sep}$. The experimental data is taken from the same shot 179838 from campaign FY2019. The ratio $\alpha = n_{e,sep} / \bar{n}_e$ varies depending on the plasma condition, and typically increases with $\bar{n}_e$, the line averaged density. Here, automated fits were used to assess $n_{e,sep}$ with a subset of detailed profile fits in the time range to adjust the separatix location based on a power balance estimate [37]. Several values of the ratio based on pedestal profile fitting are shown in Table.1. But uncertainties still exist due to the scattering of the data points. As an estimation, a linear relation is obtained: $\alpha = 0.051 \times \bar{n}_e + 0.11$, and is used in the following analysis.

$\bar{n}_e$ ($10^{19} m^{-3}$)	3.70	3.85	4.18	4.55	5.07
$n_{e,sep}$ ($10^{19} m^{-3}$)	1.1	1.21	1.35	1.55	1.88
α	0.29	0.31	0.32	0.34	0.37

Table. 1. Ratio of $n_{e,sep}$ to $\bar{n}_e$ based on pedestal profiles fitted using Thomson scattering data for shot 179838

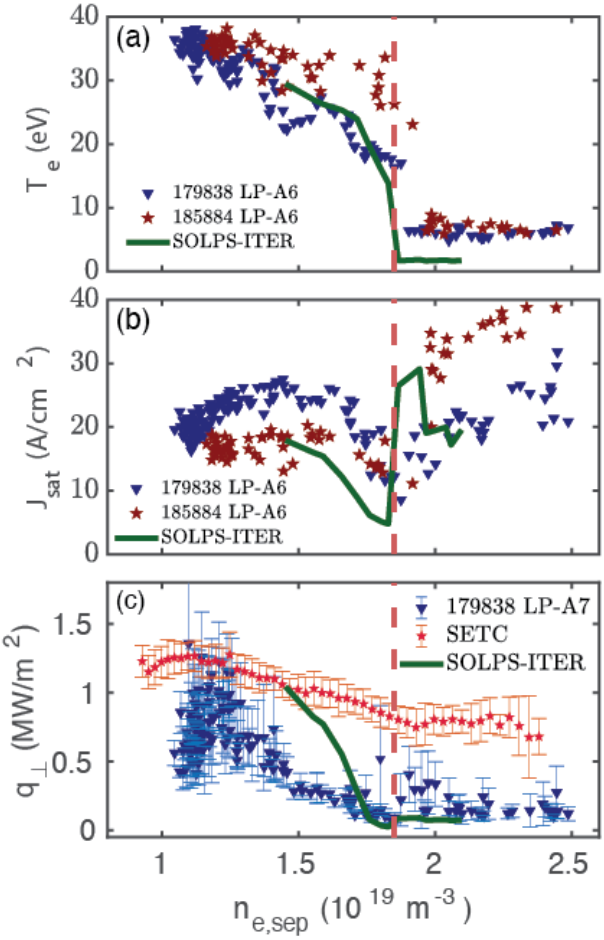

FIG. 3. (a) Electron temperature, T_e, and (b) particle flux, J_{sat}, near the strike point, measured by Langmuir probe (LP-A6) embedded in the divertor target plate, (c) deposited heat flux, $q_\perp$, at the slot bottom inferred from by Langmuir probe LP-A7 and measured by surface eroding thermocouples (SETCs) on the target, versus $n_{e,sep}$. Electron temperature, particle flux and deposited heat flux at corresponding locations from SOLPS-ITER modeling are overplotted with solid lines.

As shown in the figure, for ion **B**×∇B away from the X-point, the divertor plasma enters the highly dissipative regime above $n_{e,sep} \sim 1.85 \times 10^{19} m^{-3}$, as marked by a sharp decrease in T_e near the strike point, from around 15 eV to 5eV. The particle flux to the target near the strike point presents more complex dynamics. As upstream density increases, the J_{sat} value increases until it reaches a maximum value. Then the particle flux decreases to the minimum value, followed by a sharp increase, at the same $n_{e,sep}$ where the T_e cliff occurs. The evolution of particle flux to the target is mostly due to the change of **E**×**B** drift flues near the stripe point, which will be discussed in later section. The deposited heat flux at the bottom of the slot continues to drop with increasing upstream density until

detachment of the divertor plasma. However, the heat flux measured by the thermocouple is significantly larger than that inferred from the Langmuir probe, especially near electron temperature bifurcation. This may be due to the fact that thermocouples receive extra heat load due to radiative heating, while Langmuir probes only infer heat flux from ions. Similar experiments were conducted in the DIII-D experimental campaign FY2020. To check the consistency of the results, experimental data from shot #185884 in FY2020 is also shown in Fig. 3. The results are fairly reproducible, although the T_e cliff happened at a slightly higher upstream density.

SOLPS-ITER simulation with full drifts successfully predicts the electron temperature bifurcation, as shown in Fig. 3. The code reproduced the overall trends and key features of the experimental measurements from Langmuir probes. However, the divertor plasma is more detached with T_e around 2eV in the modeling. While the experimental data shows moderate detachment state. The deposited heat flux, $q_\perp$, from the modeling without contribution from radiation, is also significantly lower (factor of 2-4) than thermocouple measurements.

To investigate the mechanism of such bifurcation behavior of the plasma, profile evolution along the outer target in the SAS divertor of several plasma quantities including electron temperature, density and neutral density are shown in the left side of Fig. 4 for three simulation cases for increasing upstream separatrix densities (pre-T_e drop : $n_{e,sep} = 1.76 \times 10^{19} m^{-3}$, at $-$ T_e drop: $n_{e,sep} = 1.83 \times 10^{19} m^{-3}$, post $-$ T_e drop: $n_{e,sep} = 1.86 \times 10^{19} m^{-3}$) near where the T_e collapse happened. It is seen that as the upstream density increases, electron temperature decreases until a sudden collapse to $T_e \sim 2$ eV along the whole target. The electron temperature gradient also decreases. Correspondingly, significant increases of the plasma density and neutral density in the outer common flux region (CFR) are observed.

SOLPS-ITER finds that the electron temperature bifurcation is strongly associated with an **E**×**B** flow reversal in the outer CFR. The right side of Fig. 4 show radial profiles of plasma potential, radial and poloidal electric fields. Here, the plasma potential, V_p, was calculated by the SOLPS-ITER code which included the effect of the current density along the magnetic field lines, $j_{||}$, on the sheath potential and on Ohm's Law. The radial and poloidal electric field are calculated using the plasma potential: $E_r = -\frac{\partial V_P}{\partial r}$, $E_\theta = -\frac{\partial V_P}{\partial \theta}$. As show in Fig. 4 (d), the radial profile of V_P largely follows the radial variation of T_e. In attached conditions with $T_e > 15eV$, the radial electric field, E_r, causes a strong poloidal **E**×**B** flow away from the target in the outer CFR, maintaining a low density, high temperature state. As upstream density increases, plasma potential and its radial gradient start decreasing. Thus, E_r decreases as well, along with decreased poloidal **E**×**B** flow out of the divertor, which facilitates accumulation of particles near the strike point and further reduction of the electron temperature. This positive feedback process eventually leads to reversal of E_r and poloidal **E**×**B** flow, changing its direction from away from the target plate to towards the target plate.

The poloidal electric field, E_θ, in the SOL region [38-40] is also given by

$$E_\theta = -\frac{\partial \phi_p}{\partial \theta} = \frac{B_{tot}}{B_\theta}\left(\frac{j_{//}}{\sigma_{//}} - \frac{0.71}{e}\frac{\partial T_e}{\partial s_{//}} - \frac{1}{ne}\frac{\partial p_e}{\partial s_{//}}\right).$$

Here, plasma resistivity $\sigma_{//}[\mathrm{ohm}^{-1}\mathrm{m}^{-1}] \approx 3.6 \times 10^7 [T_e[\mathrm{keV}]]^{\frac{3}{2}}$ [37]. E_θ is determined by three terms, the parallel current (usually neglected in attached conditions), the parallel gradient of electron temperature and the parallel gradient of electron pressure. The contribution of the three components along the flux tube near the strike point for both attached and detached plasmas ($n_{e,sep} = 1.83$ and $1.86 \times 10^{19} m^{-3}$) is shown in Fig. 5. It is seen that before detachment, the poloidal electric field near the target due to parallel current and electron temperature gradient can be neglected. The pressure gradient term results in negative E_θ and radial **E**×**B** flow away from the target plate. As plasma density increases, electron temperature drops. Since $\sigma_{//} \sim T_e^{3/2}$, the first term with parallel current increases. In the meanwhile, the pressure gradient term decreases. Thus, the magnitude of E_θ decreases and eventually reverses its direction, causing the reversal of radial $E \times B$ flow, from away from the target plate to towards the target plate.

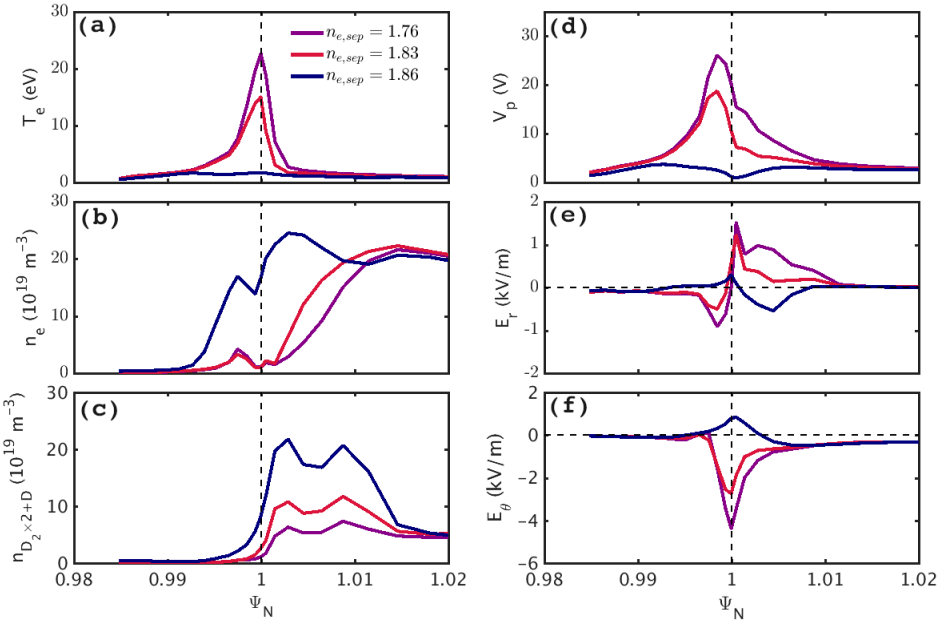

FIG. 4. Radial profiles of (a) electron temperature, T_e, (b) electron density, n_e, (c) neutral density, $n_D + n_{D_2} \times 2$, (d) plasma potential, V_p, (e) radial electric field, E_r, (f) poloidal electric field, E_θ, profiles, at the outer target in the SAS divertor for three simulation cases with different upstream separatrix density $n_{e,sep}$ near the detachment bifurcation.

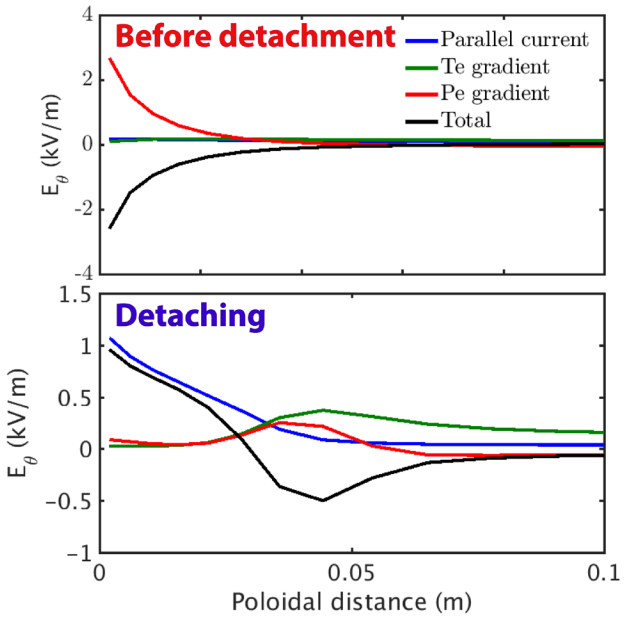

FIG.5 Poloidal electric field, E_θ, along the flux tube in SOL near the strike point due to parallel current, electron temperature gradient and pressure gradient for both attached and detaching conditions corresponding to the $n_{e,sep}$=1.83 and 1.86× 10^{19}m^{-3} cases.

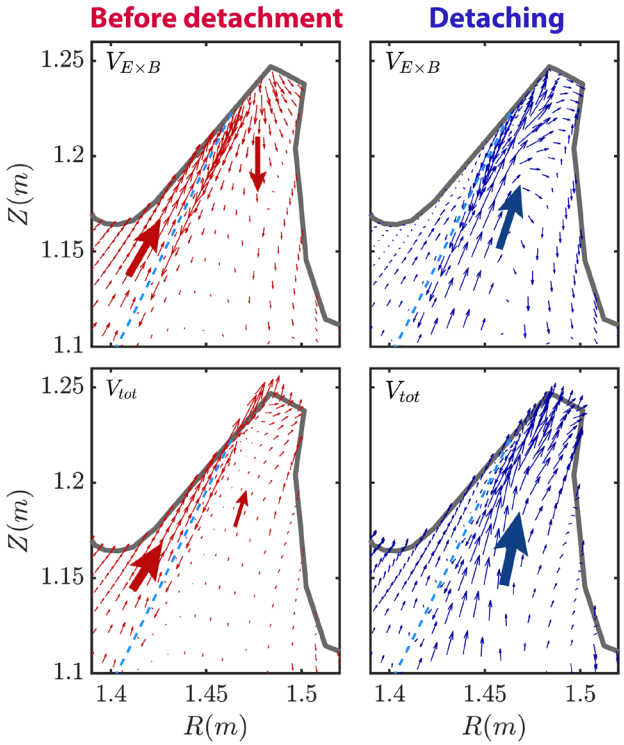

FIG. 6. Ion **E×B** velocity, $V_{E\times B}$, and ion total velocity, V_{tot}, distribution for attached and detached conditions. The size of the arrows indicates the relative magnitude of the velocity.

The **E×B** flow reversal during the divertor plasma detaching process can be clearly seen from the

velocity vector plots. Fig. 6 shows the comparison of the ion **E×B** velocity, $V_{E\times B}$, and the total velocity, V_{tot}, for two cases near the T_e cliff. Here the ion total velocity includes the **E×B** velocity, poloidal projection of the ion parallel velocity and other velocities (diamagnetic velocity, magnetic field curvature velocity, etc.). Generally, the poloidal component of the **E×B** velocity dominates. As shown in the left side of Fig. 6, before detachment, $V_{E\times B}$ is towards the target in the private flux region (PFR) and away from the target in the near-separatrix part of the outer CFR, which is in the opposite direction of the main plasma flow, resulting in smaller total plasma flow towards the target. In contrast, for the low T_e condition, the $V_{E\times B}$ flow in the near-separatrix part of the outer CFR reverses its direction, going in the same direction as the main plasma flow, resulting in much larger total plasma flow into the divertor, as shown in the right side of Fig. 6. The reversal of **E×B** flows allows a rapid density accumulation in the CFR, especially in the divertor slot, initiating detachment and leading to plasma cooling across the entire outer target. As a result, the divertor plasma shows a bifurcative step transition from low-density, high-temperature, attached conditions to high-density, low-temperature, detached conditions, as shown in both experiments and modeling.

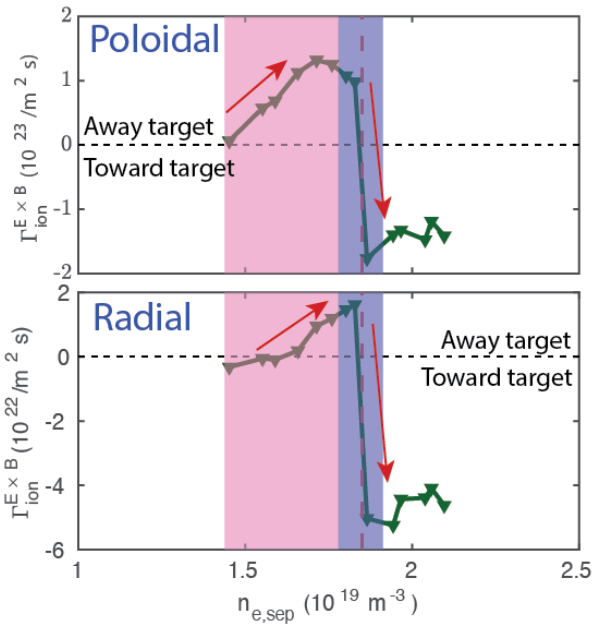

FIG. 7. Poloidal (upper) and radial (lower) E × B flux, near the strike point, calculated from SOLPS-ITER simulations, versus $n_{e,sep}$~$0.35\bar{n}_e$.

The evolution of particle flux in Fig. 3 (b) is more complex and can be inferred from the dynamics of the poloidal and radial **E×B** drift fluxes in the SOL region near the strike point as show in in Fig. 7. It is important to note that the amplitude of the poloidal drift flux is nearly one order larger than the radial drift flux. For attached conditions, both poloidal and radial **E×B** fluxes are away from the divertor plate. As upstream density increases, their amplitudes also increase, leading to decreased total particle flux to the target plates as shown in Fig. 3 (b). When the electron temperature starts dropping, the poloidal **E×B** flux decreases and reveres its direction eventually, from away from the target to towards the target. Combined with reversal of the radial **E×B** flux, a significant increase (factor of 3-4) of the total particle flux to the target is observed. This is clear evidence that **E×B** drift flows are comparable with the main plasma flow, and can strongly affect the particle recycling in the divertor region.

5. Necessary condition for detachment cliff

For the entire set of simulations discussed above, the same set of radial transport coefficient is used. To investigate the influence of the plasma profile on the impact of drifts, different set of radial transport coefficient is calculated using measured upstream n_e and T_e profiles at lower density ($\bar{n}_e \approx 4.0 \times 10^{19}/m^3$) of shot #179838 at 3800ms. Again, particle diffusivity D and electron thermal diffusivity χ_e are iterated until a satisfactory match between experimental and modeling profiles is achieved. Larger radial transport at the separatrix is achieved, with $D_{sep} = 0.3\, m^2/s$ and $\chi_{sep} = 1.0\, m^2/s$. In addition, the transport coefficients in the divertor region need to be increased by a factor of 5 for a better match to the n_e and T_e profiles along the target. Stronger radial transport in the divertor region leads to larger SOL width and broader profiles compared to the set of modeling discussed in the first part of the manuscript. Thus, smaller radial gradient leads to weaker **E×B** drift effects. The resulting target electron temperature as a function of the upstream density is compared to the previous results, as shown in Fig. 8. It is seen that the evolution of the electron temperature at the target shows a less dramatic bifurcation. It is clear that formation of such T_e cliff on a highly slanted surface favors a relative narrow SOL width with strong radial gradient near the separatrix. This result is consistent with modeling analysis of necessary conditions for a T_e cliff in the lower divertor of DIII-D with full drifts [25].

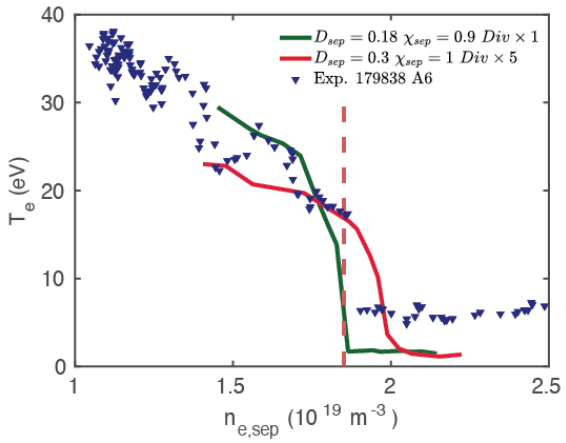

FIG. 8. Electron temperature near the strike point measured by target Langmuir probe (LP-A6) and two sets of SOLPS-ITER simulations with different cross-field transport coefficients, as a function of upstream OMP separatrix density.

6. Conclusion

In summary, a novel SAS divertor configuration has been developed to achieve divertor dissipation at lower plasma density for steady-state operation. Experiments in DIII-D and associated SOLPS-ITER modeling with full drifts find a strong synergy between drifts and divertor geometry on divertor detachment onset. The coupling of divertor geometry and drift flows can strongly affect the path towards divertor detachment onset. With the strike point on the inner slanted surface and ion **B**×∇B away from the magnetic X-point, an electron temperature bifurcation is observed with T_e suddenly falling below ~5eV both experimentally and computationally. This differs from the situation for the open divertor where the T_e cliff was only observed for normal-Bt. In the open divertor configuration, the **E**×**B** flows in the private flux region drive particles towards outer divertor from inner divertor. As plasma density increases, divertor T_e decreases, **E**×**B** flows increases non-linearly, leading to fast accumulation of plasma in the outer divertor and eventually collapse of divertor T_e. The cause of the T_e cliff in the SAS divertor is different and is mainly due to the **E**×**B** flow reversal in the SOL region. SOLPS-ITER modeling with full drifts shows that the **E**×**B** drift flows are comparable with the main plasma flow. Before divertor detachment, as upstream density increases, divertor electron temperature decreases. **E**×**B** drift flows that are away from the divertor plate decreases as well, leading to a rapid accumulation of particles in the slot. Electron temperature near the strike point is further reduced until the **E**×**B** drift flows actually reverse, with flow towards the target plate instead of away from the target plate. Enhanced total plasma flow into the divertor results in sudden collapse of the electron temperature and, driving divertor plasma towards detachment. These results indicate that the interplay between geometry and drifts needs to be fully taken into account in future fusion reactor divertor designs.

This material is based upon work supported by the U.S. Department of Energy, Office of Science, Office of Fusion Energy Sciences, using the DIII-D National Fusion Facility, a DOE Office of Science user facility, under Award(s) DE-FC02-04ER54698, DE-SC0019256, DE-AC05-00OR22725 and DE-NA0003525.

[1] P.C. Stangeby and A.W. Leonard, Nucl. Fusion **51**, 063001 (2011)
[2] P.C. Stangeby, Plasma Phys. Control. Fusion **60**, 044022 (2018)
[3] A.W. Leonard, Plasma Phys. Control. Fusion **60**, 044001 (2018)
[4] R. Pitts, et al, Nucl. Mater. Energy **20**, 100696 (2019)
[5] A.S. Kukushkin, et al, Fusion Eng. Des. **86,** 2865 (2011)
[6] D. Eldon, et al, Nucl. Fusion **57**, 066039 (2017)
[7] B. Lipschultz, et al, in Proceedings of the 16th IAEA Fusion Energy Conference in Montreal, Canada (1997)
[8] R.D. Monk and JET Team, Nucl. Fusion **39**, 1751 (1999)
[9] E. Joffrin, et al, Nucl. Fusion **57**, 086025 (2017)
[10] A. Kallenbach, et al, Nucl. Fusion **39**, 901 (1999)
[11] N. Asakura, et al, J. Nucl. Mater. **266-269**, 182 (1999)
[12] H.Y. Guo, et al, Nucl. Fusion **57**, 044001(2017)
[13] Chaofeng Sang, et al, Nucl. Fusion **57**, 056043 (2017)
[14] P.C. Stangeby and Chaofeng Sang, Nucl. Fusion **57**, 056005 (2017)
[15] H.Y. Guo, et al, Nucl. Fusion **59**, 086054 (2019)
[16] L. Casali, et al, Phys. Plasmas **27**, 062506 (2020)
[17] X. Ma, et al, Nucl. Fusion **61**, 054002 (2021)
[18] S.I. Itoh and K. Itoh, Phys. rev. Lett. **60**, 2276 (1988)
[19] F. Wagner, Plasma Phys. Control. Fusion **49**, B1 (2007)

[20] A.E. Jaervinen, et al, Phys. Rev. Lett. **121**, 075001 (2018)
[21] A.E. Jaervinen, et al, Nucl. Fusion **60**, 056021 (2020)
[22] Y. Feng, et al, Plasma Phys. Control. Fusion **44**, 611-25 (2002)
[23] A.A. Pshenov, et al, Phys. Plasmas **24**, 072508 (2017)
[24] S.I. Krasheninnikov, et al, Nucl. Mater. Energy **12**, 1061-6 (2017)
[25] H. Du, et al, Nucl. Fusion **60**, 046028 (2020)
[26]X. Bonnin et al, Plasma Fusion Res. **11**, 1403102 (2016)
[27]R. Schneider, et al, Contrib. to Plasma Phys. **46**, 3 (2006)
[28] D. Reiter, et al, Fusion Sci. Technol. **47**, 172 (2005)
[29] L. Lao, et al, Nucl. Fusion **25**, 1611 (1985)
[30] X. Ma, et al, Phys. Scr. **T171**, 014072 (2020)
[31] E. Meier, et al, Contrib. to Plasma Phys. **60**, e201900151 (2020)
[32] A.V. Chankin, et al, Plasma Phys. Control. Fusion **57,** 095002 (2015)
[33]J. Bohdansky and J. Roth, J. Appl. Phys. **51**, 2861 (1980)
[34] J. M. Canik, et al., J. Nucl. Materials **415**, S409–S412 (2011)
[35] J.M. Canik, et al, Phys. Plasm*as* **24**, 056116 (2017)
[36] L. Casali, et al, *Phys. Plasmas* **27**, 062506 (2020)
[37] A.W. Leonard et al., *Nucl. Fusion* **57**, 086033 (2017)
[38] T. D. Rognlien, D. D. Ryutov, N. Mattor, and G. D. Porter, Phys. Plasmas **6**, 1851 (1999).
[39] P. C. Stangeby, The Plasma Boundary of Magnetic Fusion Devices (Taylor & Francis, London, 2000).
[40] S. I. Braginskii, in Reviews in Plasma Physics, edited by M. A. Leontovich (Consultants Bureau, New York, 1965), Vol. 1, p. 205.